Simulation Insights on the Structure of Nanoscopically Confined Poly(ethylene oxide)

V. KUPPA,[1] S. MENAKANIT,[1,2] R. KRISHNAMOORTI,[3] E. MANIAS[1]

[1]Department of Materials Science and Engineering, The Pennsylvania State University, 325-D Steidle Building, University Park, Pennsylvania 16802

[2]Ceramic Industry Development Center, Lampang 52130, Thailand

[3]Department of Chemical Engineering, University of Houston, 4800 Calhoun Avenue Houston, Texas 77204

ABSTRACT: We employ atomistic computer modeling to investigate the structure and morphology of poly(ethylene oxide) (PEO) chains confined in 1-nm slit pores defined by montmorillonite silicate layers. Molecular dynamics computer simulations reveal the Li^+ cations to be located in the immediate vicinity of the silicate surfaces and PEO to adopt highly amorphous conformations in a liquidlike bilayer across the slit pores. Despite the orienting influence of the parallel stacked silicate walls, PEO shows no indication of crystallinity or periodic ordering; in fact, for all temperatures simulated, it is less ordered than the most disordered bulk PEO system. These amorphous PEO film configurations are attributed to the combination of severe spatial confinement and the strong coordination of ether oxygens with the alkali cations present in the interlayer gallery. These conclusions challenge the picture traditionally proposed for intercalated PEO, but they agree with a plethora of experimental observations. Indicatively, the simulation predictions are confirmed by wide-angle neutron scattering and differential scanning calorimetry experiments on PEO/montmorillonite intercalates. © 2003 Wiley Periodicals, Inc. J Polym Sci Part B: Polym Phys 41: 3285–3298, 2003

Keywords: polymer/inorganic nanocomposites; nanoscopically confined polymers; molecular modeling; poly(ethylene oxide) (PEO); wide-angle neutron diffraction

INTRODUCTION

Polymers intercalated in layered inorganic compounds, such as graphite, 2:1 aluminosilicates, and transition-metal halides, have recently attracted very strong interest. Besides their obvious potential for industrial applications as a novel class of composite materials,[1] they are also of high scientific value as model systems for nanoscopically confined polymers.[2] Because these systems self-assemble in highly ordered intercalated structures, it is easy to prepare samples with macroscopic quantities of severely confined polymers so that conventional analytical techniques such as solid-state NMR, dielectric spectroscopy, and X-ray and neutron diffraction studies can be successfully applied.[2–11] Such experimental investigations combined with simulation studies[12–17] unveil a striking picture for the physics of polymers in severe confinements between solid surfaces.

The structure and dynamics of polymers in nanoscopic confinements exhibit complex and involved behaviors, even for the simplest cases, and they do not intuitively follow the phenomenology developed for conventional/macroscopic compos-

ites. For the system in focus here, that is, 1-nm-thick poly(ethylene oxide) (PEO)/Li$^+$ films confined between montmorillonite (MMT) platelets,[3–8] a complete understanding of the segmental relaxations, chain dynamics, and the structural arrangement of the polymer layers still remains largely elusive despite numerous experimental and simulations studies.[2–8,12–14] Despite the severe confinement the system dynamics, Li$^+$ and PEO segmental, are very rich, characterized by a coexistence of ultraslow and ultrafast dynamics across all temperatures examined,[6,8,13,14] with the temperature affecting only the relative population of fast–slow species.[13,14] On the structure, the current opinion is that PEO arranges in the interlayer gallery in an amorphous bilayer parallel to the confining clay platelets, with Li$^+$ cations located in the immediate vicinity of the solid surfaces. This structural description is supported by experimental findings[7] and also by simulations[12,13] but contradicts the traditional viewpoint of extended crystalline PEO chain conformations with the Li cations located in the centers of the films [e.g., ref. 5 (Fig. 4) or ref. 18].

Here, we performed a molecular modeling study to comparatively explore intercalated and bulk PEO systems. Specifically, molecular dynamics (MD) simulations follow the system trajectories over short timescales (a few nanoseconds), focusing on elucidating how the 1-nm confinement affects the structure of PEO. Indicatively, our simulation insights are compared against wide-angle neutron diffraction (WAND) and differential scanning calorimetry (DSC) studies of purely intercalated PEO in MMT.

EXPERIMENTAL

WAND

Neutron powder diffraction data were collected with the BT-1 32 detector neutron powder diffractometer at the National Institute of Standards and Technology Center for Neutron Research reactor, NBSR. A Ge(311) monochromator with a 75° takeoff angle, $\lambda = 2.0790(2)$Å, and inpile collimation of 7 min of arc were used. Data were collected over the 2θ range of 5.4–148°, with a step size of 0.05°. The samples were sealed in a vanadium container of length 50 *mm* and diameter 6 *mm* inside a dry He-filled glovebox. A closed-cycle He refrigerator was used for temperature control.

DSC

DSC was performed in a PerkinElmer DSC7 at a 10 °C/min heating (or cooling) rate under argon atmosphere. Experiments were done by first melting the samples at 100 °C for 3 min. Then, after quenching to the desired crystallization temperature, they were held at this temperature for 7 min to allow complete crystallization, and the temperature was then raised at a rate of 10 °C/min to quantify the melting enthalpy.

SIMULATION DETAILS

Our approach involves MD simulations of fully atomistic models of PEO oligomers intercalated in Li$^+$ MMT. A force field developed in earlier simulations of Li$^+$/PEO by Smith et al.[19,20] was used here to model PEO and Li; the PEO/MMT interactions were modeled after those used by Hackett et al.[12] The detailed force field, including both PEO and MMT parameters, is given elsewhere.[13]

Because of the existence of charges (in the silicate platelets and the neutralizing Li$^+$), as well as high partial charges in the PEO chains, the electrostatics strongly affect the system behavior. Thus, it is imperative to obtain an accurate calculation of the coulombic forces that faithfully reproduces the response of the real systems.[6,8,13,14] To this end, we evaluated various techniques for estimating the long-range electrostatic interactions, and the generalized reaction field (GRF) method[21] proved to be the most accurate and fast method for these highly charged systems.[13] For the GRF calculations, an effective dielectric constant of 3.0 was used beyond a cutoff distance of 1.0 nm.

For the confined systems, constant NVT simulations were performed at four different temperatures (273, 323, 373, and 423 K). Periodic boundary conditions were used in all three directions, with a box size of 3.696 × 3.656 × 3.558 nm, containing two MMT surfaces parallel to the *xy* plane (Fig. 1). The spacing between the MMT surfaces was chosen to match the experimental systems, which self-assemble in an extremely well defined superstructure of 0.87-nm thin PEO films,[8] and the number of PEO and Li$^+$ atoms follow the experimental values of the organic density and the MMT charge-exchange capacity, respectively. The simulation box contains two PEO/Li$^+$ films intercalated between two inorganic MMT layers, as shown in Figure 1, with 23 PEO

hexamers and 21 Li$^+$ per MMT wall. This "double-slit" geometry was chosen because it allows for more accurate electrostatic calculations.[22]

For the bulk, constant NPT simulations at six temperatures (273, 298, 323, 373, 398, and 423 K) were performed, in a manner similar to those described in refs. 19 and 20, with a cutoff radius of 0.9 nm and a distance-dependent dielectric constant.[23] The initial simulation box size was chosen to match the average PEO density to experimental values[24] at each temperature. Periodic boundary conditions were used in all three directions. All simulation boxes contained eight Li$^+$I$^-$ pairs solvated by 69 PEO hexamers.

Pressure and temperature were stabilized by a weak coupling to the reference values, via the Berendsen method.[25] The time step in all simulations was 1 fs. Well-equilibrated initial configurations were chosen from the output of previous simulations.[12] Typically, after an initial energy minimization, equilibration MD runs of 10 ns were performed for all temperatures followed by productive runs of 2–6 ns, depending on temperature. Long equilibration runs were required for the convergence of dynamics to a steady state [characteristic of the force field (electrostatics) and the temperature], namely, stabilization of the diffusion mechanisms and constants.[13,14] The structural properties, which this article focuses on, equilibrate much faster (within 4–5 ns); for example, the relaxation of the end-to-end vector ($\tilde{u}$) for PEO chains in confinement, which is the structural property with the longest equilibration
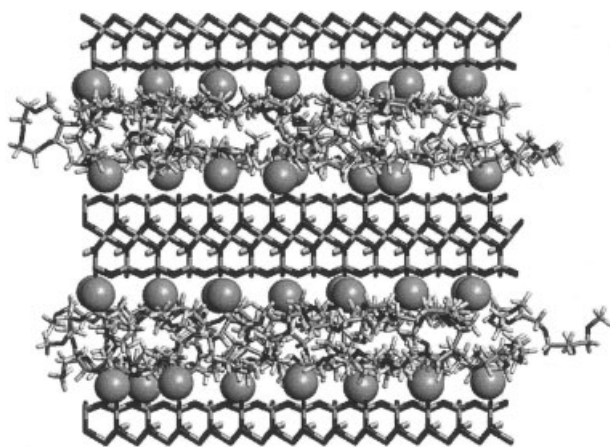

Figure 1. Simulation box with double-slit geometry. Li$^+$ ions are represented by their van der Waals spheres to clearly show their positions with respect to the inorganic walls.
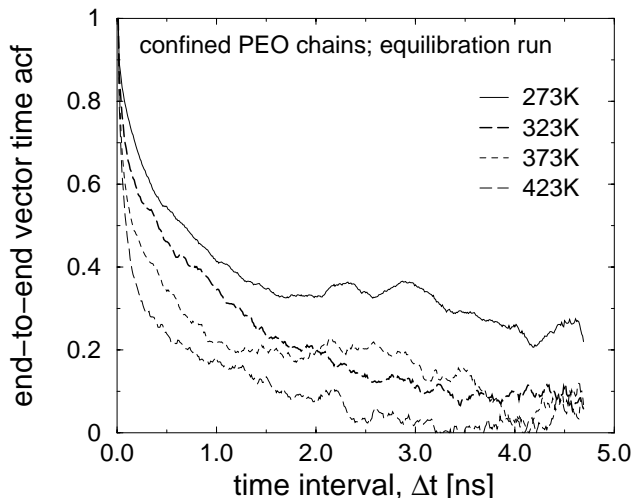

Figure 2. End-to-end vector time autocorrelation function, $\langle \tilde{u}t \rangle \cdot \tilde{u}(0) \rangle$, for the confined PEO chains for all temperatures as an example of the structural equilibration of the systems. This is the "structural" quantity with the longest equilibration time, relating to the relaxation of the chain conformations.

time, is depicted in Figure 2, through its time autocorrelation function.

RESULTS AND DISCUSSION

Lithium in the MMT Gallery

Because of isomorphic substitutions, MMT-layered silicates bear a net negative charge; in their pristine form this charge is counterbalanced by hydrated cations (Na$^+$, Li$^+$, and Ca^{2+}) that exist in the interlayer. During the nanocomposite formation, Li$^+$ is typically used to exchange all the pristine cations, and subsequently PEO chains replace the water in the interlayer.[8] In the resulting intercalated structures, the lithium counterion positions are dictated by the system interactions, namely, the electrostatic attractions from the negative MMT layers and the coordination to the PEO and silicate oxygens.

The balance between these competing forces determines the spatial arrangement of the lithium cations. Our simulations reveal that the electrostatic attraction of MMT and the coordination of the Li$^+$ with the oxygens on the silicate surface overwhelm the PEO coordination, and the lithiums are located in close proximity to the MMT surfaces (Fig. 3), residing in the hexagonal pockets of lower energy defined by the MMT surface oxygens.[13] To quantify this coordination behavior, we calculated
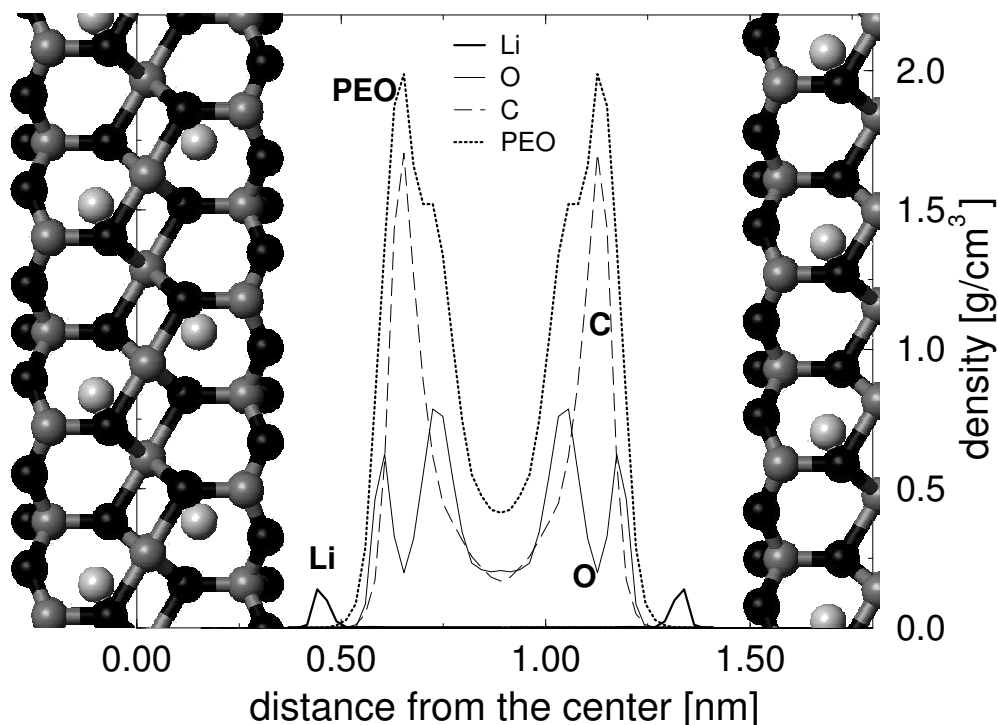
Figure 3. One dimensional mass density profiles across the slit pore. The Li and total PEO density distributions are shown as well as the oxygen and carbon distributions.

the Li^+/oxygen coordination numbers in the bulk PEO systems, as well as in the intercalated systems (Table 1). These coordination numbers were calculated by the integration of the first peak in the lithium–oxygen radial distribution functions. A comparison between the bulk and confined systems revealed a higher number of coordinated oxygens in the confined systems because the Li^+ can maximize their coordination next to the highly packed oxygens of the crystalline MMT surface. At the same time, this lithium arrangement at the MMT/PEO

interface reduces markedly the PEO-oxygen/Li^+ coordination as compared to the bulk systems[26–29] because, due to the geometric constraints, PEO only exists in one half of the space around the Li^+. Despite the fact that each Li is coordinated on average with fewer PEO oxygens (Table 1), in total PEO is

Table 1. Coordination Numbers of Li^+ with Oxygen of PEO Backbone in Bulk Li^+I^-/PEO and with Oxygens of PEO Backbone and Oxygens of the Silicate Surface in Confined Li^+MMT/PEO

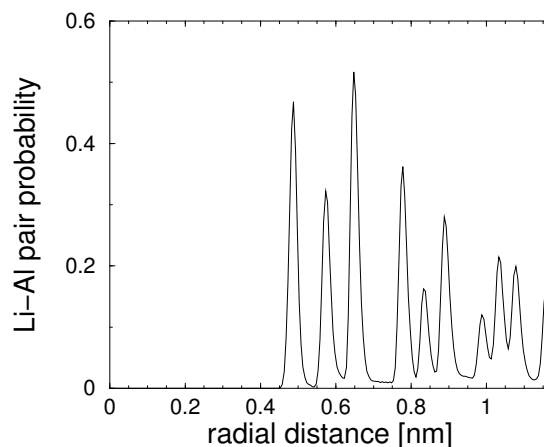| | Bulk | Confined | |
| | O_{PEO} | O_{PEO} | O_{MMT} |
$T(K)$			
273 (6ns)	6.16	3.62	5.68
298 (4ns)	6.24	–	–
323	6.25	3.61	5.82
373	6.27	3.45	5.89
398	6.13	–	–
423	6.07	3.45	5.92

Figure 4. Lithium–aluminum pair probability as a function of radial distance. Li^+ ions are located in the interlayer gallery, whereas Al^{3+} ions reside in central octahedral sites in the middle of the silicate layer structure.

very highly coordinated to the Li^+ in the confined systems because of the much higher O:Li ratio (6.6:1 in the confinement as opposed to 52:1 in the bulk).

Such a lithium arrangement dictates that the Li^+ are very close to the silicate surface (Fig. 3). This fact enables analytical techniques, such as solid-state NMR experiments probing [7]Li spectra, to estimate the location of the Li in the intergallery. Namely, the presence of paramagnetic Fe impurities in the octahedral Al positions of the silicate lattice induce a line broadening in the [7]Li spectrum. Analysis of this phenomenon[7] estimated the minimum distance between the Li^+ and the layer of Al^{3+} in the silicate to be about 0.45 nm.[6,7] This NMR quantification can be compared with our MD simulations (through the calculation of the probability distribution function between Li^+ and Al^{3+}; Fig. 4). As seen in Figure 4, the foot of the first peak in the distribution, which corresponds to the minimum distance between Li^+ and Al^{3+}, is at 0.45 nm, in agreement with the experimental results. Because the lithium position is very sensitive to the forces acting on the lithium by the silicate layer and the intercalated PEO, correctly locating the Li^+ in the interlayer gallery serves as an important sensitive check of the validity of our simulation technique and force field. Finally, such a lithium arrangement, in close proximity to the MMT surfaces, originates from the high negative charge of the MMT layers. Studies performed on PEO intercalated in non-charged inorganic layers (like transition metal halides, e.g., $RuCl_3$ and TaS_2) locate the lithiums at different positions across the slit pore, typically in the middle of the intercalated PEO film.[9, 30]

Structure of Intercalated PEO

Electron Densities

The structures of 2:1 aluminosilicates nanocomposites, formed by the intercalation of PEO within the silicate layers, have long been experimentally probed with techniques such as neutron scattering and X-ray diffraction (XRD). These reciprocal space techniques provide little, if any, information about the PEO conformations in the intergallery. It is possible to calculate a one-dimensional (1D) electron density across the c crystallographic axis from the relative intensities of the 00n XRD reflections. In most cases, an accurate calculation necessitates more than 12 00n peaks, but given the experimental difficulties of
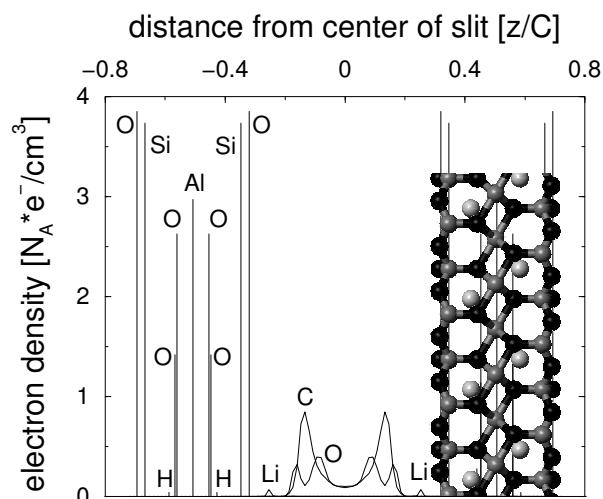

Figure 5. One dimensional electron density profiles across the slit pore. The distance is normalized by the d-spacing of the intercalate ($C = 1.8$ nm).

obtaining peaks of such high order (and given the very small intensities of peaks beyond the 006), even the most precise experimental approaches only use the first five to seven 00n reflections.[9,31] Even more often, no estimations were made for the PEO conformations; instead, crystalline helical conformations were assumed in the intercalated films, a postulation usually biased by the misleading coincidence of the thickness of a helical PEO arrangement and the thickness of the intercalated PEO films (both were *ca.* 0.8 nm).

This traditional picture, assuming crystalline PEO arrangements in intercalated films, is challenged by the experimental facts; never has there been a melting point associated with purely intercalated, that is, no polymer outside the intergalleries, PEO systems, neither have there ever been crystalline diffraction peaks from purely intercalated PEO, despite numerous XRD and WAND studies. Molecular simulations can be an invaluable tool to complement the experiments because they provide a detailed atomistic picture of these systems. Figure 5 shows the ensemble averaged 1D electron densities that were calculated from our simulations. These 1D electron densities (in the 001 crystallographic direction) compare favorably with experimentally derived (from 00n XRD fits) electron densities for PEO intercalated in MMT^{31} and in other layered hosts (e.g., $RuCl_3$[9] and V_2O_5[32]), as seen in Figure 6. Moreover, the simulated electron density that corresponds to a disordered bilayer captures far better the experimental trends than the electron density that cor-
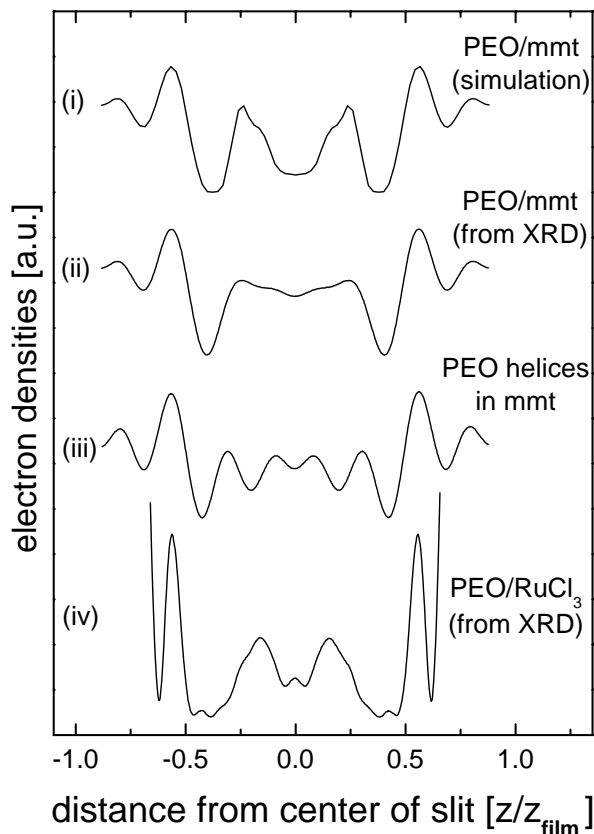
Figure 6. Total 1D electron-density profiles across the slit pore. The distance is normalized by the respective film thickness of the intercalated PEO film (z_{film}). From top to bottom, the electron densities are: (1) as enumerated by these simulations, (2) as derived by fits of the 00n XRD reflections of PEO in MMT,[31] (3) as derived by assuming crystalline (helical) PEO conformations in the intercalated slit, and (4) as derived by fits of the 00n XRD reflections of PEO in $RuCl_3$.[9]

responds to a crystalline/helical PEO arrangement (Fig. 6).

Starting with the electron densities, we can proceed to compute the diffraction peak intensities (see Appendix) of these "infinitely" periodic PEO intercalates (Fig. 7), as defined by the repetition of our simulation box across the periodic boundary conditions. These simulated systems would best compare against aligned nanocomposites cast from solution, in which case the XRD patterns display several order of 00n reflections.[9,31–33] As can be seen (Fig. 7), our results reproduce well the XRD patterns from experiments. Thus, the disordered bilayer PEO arrangement in the interlayer can quite adequately account for the experimental diffraction peaks and their relative intensities (Fig. 7 inset).

The implications of such an analysis are twofold. First, the amorphous bilayer morphology revealed by our MD studies was consistent with the experimental XRD results. Second, this agreement was not limited to PEO/MMT systems but described well other intercalated PEO films: as seen in Figures 5 and 7, there is agreement with the XRD results from PEO in hectorite[33] (a naturally occurring clay) and PEO in $RuCl_3$ and in V_2O_5[9,32] (both synthetic-layered crystals). This revealed that rather than clay/PEO surface chemistry, it is the confinement that dictates the intercalated PEO morphology. Expanding from this viewpoint, the intercalated 0.87nm-wide bilayer films are the most stable PEO arrangement from steric considerations[34] and as has been experimentally demonstrated, disordered bilayers are the most stable arrangements for all organics and polymers examined by the surface forces apparatus[35] between mica surfaces. In this context, a
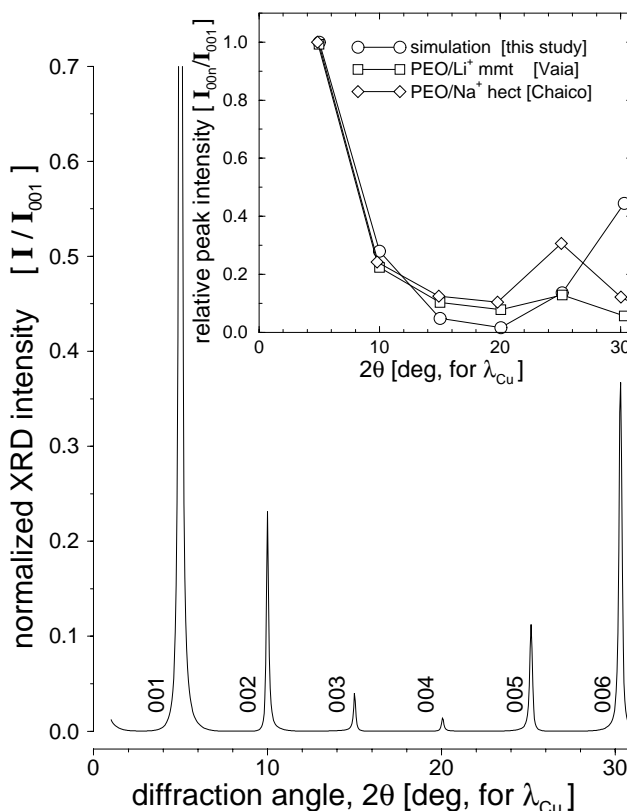

Figure 7. Simulated XRD pattern for nanocomposite of PEO/Li^+ MMT, corresponding to a perfectly intercalated PEO/MMT system, as defined by the repetition of the simulation box through the three-dimensional periodic boundary conditions. Inset compares the relative intensities (I_{00n}/I_{001}) for three different XRD patterns: simulated PEO/Li^+ MMT (this work), experimental PEO/Li^+MMT,[31] and experimental PEO/Na^+hectorite.[33]

Table 2. Ensemble Averaged Order Parameters for the Bulk and Confined PEO Systems as a Function of Temperature

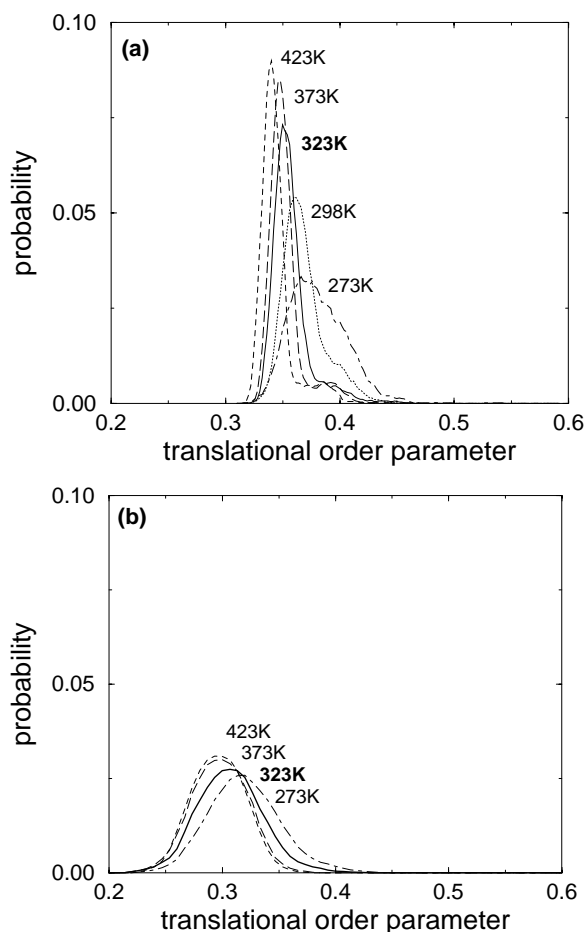| Translational Order				Orientational Order				Crystalline Order			
Bulk		Confined		Bulk		Confined		Bulk		Confined	
T (K)	$\langle \tau \rangle$	T (K)	$\langle \tau \rangle$	T (K)	$\langle q \rangle$	T (K)	$\langle q \rangle$	T (K)	$\langle Q_6 \rangle$	T (K)	$\langle Q_6 \rangle$
273	0.38	273	0.33	273	0.67	273	0.58	273	0.44	273	0.25
298	0.37	—	—	298	0.67	—	—	298	0.46	—	–
323	0.37	323	0.33	323	0.66	323	0.58	323	0.47	323	0.24
373	0.35	373	0.33	373	0.66	373	0.58	373	0.47	373	0.25
398	0.35	—	—	398	0.66	—	—	398	0.46	—	–
423	0.35	423	0.32	423	0.66	423	0.58	423	0.46	423	0.24

disordered bilayer is not only justified, but necessary.

Order Parameters

Even for the very short oligomers simulated here that are incapable of forming extended crystalline arrangements (e.g., spherulites), MD simulations recorded a qualitative change in the structure and dynamics of the bulk PEO systems as the temperature crossed the melting point of PEO (*ca.* 323 K). These changes manifested themselves both in the chain conformations as well as the ordering of the chain molecules.[14] Differences between the ordering of the bulk and the confined chains simulated provided clues about the origins of the confinement-induced structural features in nanoscopically confined PEO.

To quantify the ordering of the chain molecules at different temperatures, we used three different order parameters measuring the regular/periodic arrangement of the atoms in the system. The first parameter (parameter of translational order) measures the periodic stacking of the PEO chains, the second (parameter of orientational order) measures the atomistic tetrahedral arrangement, and the third (Q_6) measures the overall periodicity in the organic film. Although for the first two-order parameters a particular periodic arrangement is assumed, the third order parameter is independent of the crystalline symmetry that the chains may rearrange in. The first two parameters were used in a recent computer simulation study of water,[43] and the third was used in the modeling of crystal nucleation.[44]

The parameter of translational order (τ) is defined by

Figure 8. Parameter of translational order distributions for carbon atoms (a) in bulk PEO and (b) in the confined systems.

$$\tau = \frac{\int_0^{\xi_c} |g(\xi) - 1| d\xi}{\xi_c} \qquad (1)$$

where ξ is the normalized radial distance between carbon atoms ($\xi = r\rho^{1/3}$, where r is the carbon radial distance, and ρ is the carbon number density), $g(\xi)$ is the interchain radial distribution function of the carbons in the simulation cell, and ξ_c is a cutoff distance whose maximum value is determined by the size of the simulation box. In our case, for both the bulk and the confined systems the cutoff was chosen as half of the smallest box dimension. To a first approximation, τ is a measure of the normalized periodic separation/ spacing between interchain carbons in the system. It is thus a scalar parameter indicative of the stacking periodicity between adjacent chains. Values for τ varied between 0 and 1, with lower values reflecting no preferential spacing ($\tau = 0$ corresponds to an ideal gas) and higher values indicating a tendency toward crystallinity ($\tau = 1$ would be a perfect crystal structure).

τ, as defined above, is an average scalar quantity for the entire system (Table 2). In our study, we also wanted to examine the stacking periodicity around each carbon in the PEO chains. Toward this purpose, we determined the interchain carbon–carbon radial distribution functions [rdf, $g_i(r)$] for each individual carbon atom i, and we calculated a τ_i for each carbon with its respective rdf. Such an analysis gives us a distribution of translational order parameters for the carbon atoms as a function of temperature for bulk and confined systems as shown in Figure 8. The mean value, $\langle \tau \rangle$, was obtained by averaging the distribution over all the carbon atoms (i) in the system and was equivalent with eq 1 when calculated across the simulated ensemble.

For the bulk systems, $\langle \tau \rangle$ decreased with temperature, indicating that as the temperature is raised the tendency for the oligomers to orient in a crystalline fashion decreases [Fig. 8(a)]. Moreover, the distribution became narrower as the temperature increased because regions of periodic packing (high-τ peak) disappeared, and the system became disordered throughout. For the confined system there was no marked change in the order parameter $\langle \tau \rangle$ with temperature, albeit a small change in the width of the distribution [Fig. 8(b)]. When comparing the translational order parameters for the bulk and confined systems, for the confined chains $\langle \tau \rangle$ was lower than the bulk value (independent of temperature). This difference in $\langle \tau \rangle$ indicated that the spatial order in the confined system was reduced as compared with the bulk polymer, despite the ordering effect imposed by the confining solid surfaces. Furthermore, the confined systems appeared more disordered than the bulk systems for all the temperatures simulated, even when compared with the most amorphous bulk at the highest temperature.

In addition to τ defined previously (which studies the translational regularity of adjacent particles), a more complete description of the chain arrangements can be obtained by quantifying also the orientational order in the systems. The parameter of orientational order (q) is defined as follows, with a definition paralleling that of ref. 45.

$$q_i = 1 - \frac{3}{32} \sum_{j=1}^{3} \sum_{k=j+1}^{4} \left(\cos \psi_{j,i,k} + \frac{1}{3} \right)^2 \qquad (2)$$

where $\psi_{j,i,k}$ scans all the angles centered on an oxygen atom i and defined by all pairs (j, k) of its four nearest interchain oxygen neighbors. The numerical factors used normalized the value for q_i between 0 and 1 (with 1 corresponding to a perfect tetrahedral arrangement centered around the ith oxygen). The physical significance of q is that it quantifies the quality of tetrahedral orientation of the four nearest interchain oxygens. Thus, from the definition of q through eq 2, high $\langle q \rangle$ values indicate an orientation close to a tetrahedral structure (for a perfect tetrahedron centered around each oxygen $\langle q \rangle = 1$), lower values correspond to increasing disorder, and $\langle q \rangle = 0$ corresponds to an ideal gas, that is, a completely random oxygen orientation.

Both in the bulk and confined systems, the parameter of orientational order q was calculated by considering the angles defined by each oxygen and its four nearest interchain oxygen neighbors, that is, four nearest oxygens not belonging to the same chain. For the bulk system [Fig. 9(a)], $\langle q \rangle$ decreased with temperature, with a marked change in the distribution of q at 323 K. This means that the PEO oxygen atoms tended to lose orientational order with increasing temperature, with a distinct change in orientational order at about 323 K. For the confined chains [Fig. 9(b)], the $\langle q \rangle$ values were systematically lower than the bulk values, independent of temperature; thus, as with the translational order, the confined systems were more orientationally disordered than the bulk, even when compared to the most disordered
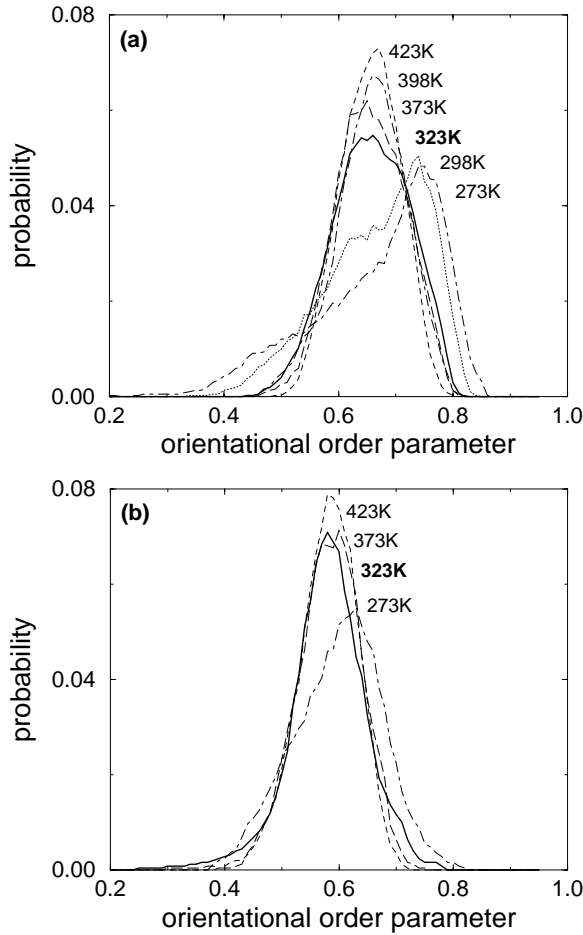
Figure 9. Parameter of orientational order distributions for oxygen atoms (a) in bulk PEO and (b) in the confined systems.

entation of the crystal in space. It can be calculated as follows.

All the neighbors j of a particular particle i within a radius r_q were identified. The position vectors $\mathbf{r}_{ij}$ between neighbors were then normalized to unit vectors $\hat{\mathbf{r}}_{ij}$, and their polar and azimuthal angles θ_{ij} and ϕ_{ij} were determined. The local structure around particle i was characterized by its order parameter $\bar{q}_{lm}$, which was constructed with the spherical harmonics $Y_{lm}(\theta_{ij}, \phi_{ij}) = Y_{lm}(r_{ij})$ as follows

$$\bar{q}_{lm}(i) = \frac{1}{N_b(i)} \sum_{j=1}^{N_b(i)} Y_{lm}(\hat{\mathbf{r}}_{ij}) \tag{3}$$

where the summation is performed over all $N_b(i)$ neighbors of particle i. In this case, $\bar{q}_{lm}$ is a local order parameter, obtained for each i. The *global* order parameter $\bar{Q}_{lm}$ is calculated by the ensem-

bulk PEO at the highest temperature simulated. Moreover, the q distribution for the confined PEO was markedly insensitive to temperature [Fig. 9(b)], suggesting that the orientational disorder remained at the same level throughout the temperatures examined [much like the translational order in these same systems, Fig. 8(b)].

The two aforementioned parameters of order were designed to probe specific aspects of the regular arrangement of PEO molecules in space. Because one can envision that PEO can adopt a different ordering behavior under confinement, as compared with the bulk PEO, we also explored a third-order parameter that can serve as a generic crystallinity index.[44] For this purpose, we followed the same approach as first used by Stenhardt et al.[46] and later by Frenkel et al.[44] in studies of crystalline nucleation. In addition to being independent of the crystal symmetry, this order parameter was also not affected by the ori-
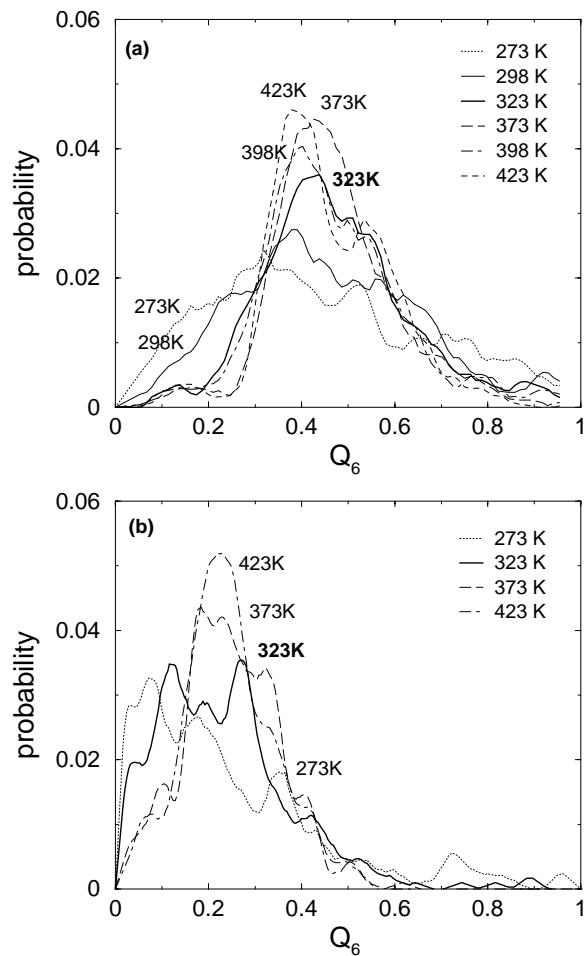

Figure 10. Rotationally invariant order parameters for oxygen atoms (a) in bulk PEO and (b) in the confined systems.

ble average over all particles and configurations, thus:

$$\bar{Q}_{lm} = \frac{\sum_{i=1}^{N} N_b(i) \, \bar{q}_{lm}(i)}{\sum_{i=1}^{N} N_b(i)} \qquad (4)$$

Obviously, $\bar{Q}_{lm}$ as defined above is still dependent on the choice of reference frame. To obtain rotationally invariant equivalent parameters (Q_l), we average over all m directions[44]

$$Q_l = \sqrt{\frac{4\pi}{2l+1} \sum_{m=-l}^{l} |\bar{Q}_{lm}|^2} \qquad (5)$$

In a noncrystalline liquid the correlations dissipate rapidly, and values of Q_l tend to be small, with a value of zero corresponding to absolute disorder, that is, a complete lack of any correlation, a situation corresponding to a disordered liquid. Most approaches use only the Q_6 parameter as a generic measure of crystallinity because Q_6 is largely insensitive to any particular crystal symmetry. As for all Q_l, Q_6 is zero for disordered states and increases in magnitude for more crystalline arrangements, where correlations through the structure develop; for pure crystals Q_6 adopts values of the order of 1.0 (calculated values of Q_6 for different crystalline structures[44] range from 0.5 for various cubic (sc,fcc) and hexagonal close-packed structures, to 0.66 for icosahedral symmetry). In Figure 10(a,b), the *distributions* of Q_6 are plotted, calculated with eq 5 for each individual oxygen in the system, for bulk and confined polymer. The $\langle Q_6 \rangle$ for both systems can be defined as the ensemble average of the Q_6 for all oxygens (Table 2).

For the bulk, the distribution for Q_6 narrows with increasing temperature, with a marked change in shape at 323 K. However, for the confined PEO chains, Q_6 have lower values than the respective bulk at all temperatures, with no clear change in the distribution shape as the temperature is increased. This implies that at all temperatures there is a confinement-induced suppression of any periodic structure. In addition, as compared with the bulk systems, the confined PEO chains showed a greater inhomogeneity in structural arrangements, as evident from the lower values of Q_6 for *all* temperatures. Thus, even the most disordered bulk polymer configuration (at 423 K) showed more order than any (273–423 K) of the confined PEO systems.
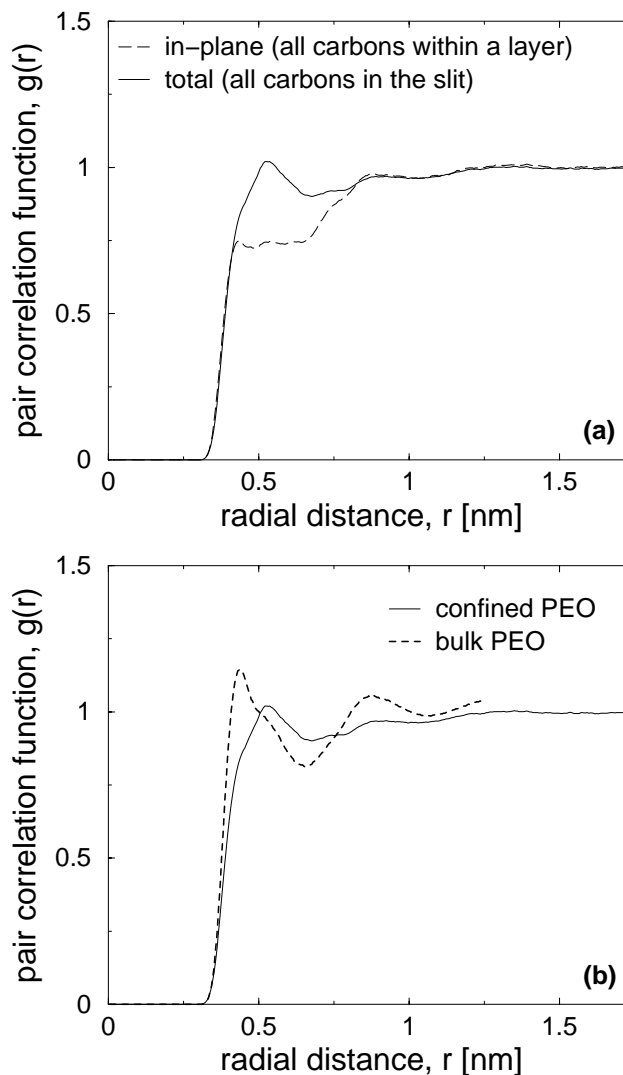

Figure 11. (a) Interchain radial distribution functions calculated in the confinement for all carbon atoms within a single slit (total), and within one of the layers (in-plane). Both these rdfs remained invariant throughout the simulated temperature range (273–423 K). (b) Interchain carbon–carbon radial distribution functions compared for polymer chains in bulk and in confinement, at one representative temperature (423 K).

When comparing the three parameters of order, that is, translational, orientational, and rotationally invariant, between the bulk and nanoscopically confined chains, it is clear that the confined chains are more amorphous/disordered than the most disordered bulk system over the entire temperature range examined despite the "flattened" chain arrangements imposed by the solid surfaces. This behavior is attributed to the severe (0.87 nm) confinement (and to a lesser extent to the coordination of the oxygens of PEO to the numerous Li^+ cations near the silicate surfaces,

which also promote highly disordered crownlike conformations[47]). Moreover, there is no marked temperature dependence of the structural order for the confined systems—in contrast with the behavior of the bulk equivalents. This is in concert with (a) the absence of any measurable phase transitions from intercalated PEO[4] and (b) the absence of any qualitatively change/transition of the PEO segmental dynamics or the Li motion.[8,13,14]

Radial Distribution Functions

Our aim in this work was to explore the structure of nanoscopically confined—intercalated—PEO and compare it to the structure of the respective bulks. In this regard, to demonstrate that the disordered structure in the intercalates are actually confinement induced, we also examined the radial distribution functions of the polymer carbons (which can be measured through the structure factors of small-angle neutron scattering experiments). For the confined system, because of the severe spatial restriction (ca. 1 nm), the chains were forced to arrange in a different manner than that of the bulk, and the rdfs of the chains in the slit pore should show different characteristics.

We first considered the interchain carbon–carbon radial distribution function [rdf, $g(r)$] within each of the two confined layers in the slit pore [Fig. 11(a)]. These rdfs revealed that there is no particular inplane arrangement of carbons within the same layer. If we subsequently enumerate the total rdf for all carbons in the slit [Fig. 11(a)], a first-neighbor peak becomes prominent, reflecting the contribution from out-of-plane carbons (i.e., the two-layer arrangement within the slit pore). This is also confirmed by the fact that the average z separation between layers, as calculated from the mass-density profile across the confinement, is approximately 0.52 nm, the same distance as the first peak in the total rdf. The comparison of the inplane and total rdfs in the confined film trace the origin of the single feature in the total rdf under confinement, which relates to the bilayer structure of the confined PEO. The rdf independence on temperature is not due to "freezing" of the polymer dynamics, imposed by confinement or strong—Li mediated—physisorption; in fact, the confined PEO chain dynamics adopt a wide distribution of relaxation times, including large populations of monomers that move *much faster* than the respective bulks at the same temperatures (e.g., see ref. 14 for a detailed discussion of the PEO dynamics in these confinements).
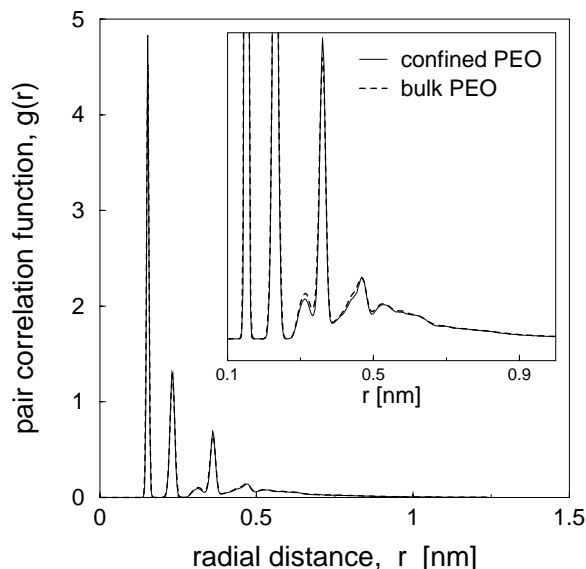

Figure 12. Intrachain carbon–carbon radial distribution functions calculated for polymer chains in bulk and confinement, at one representative temperature (423 K).

When this confined rdf is compared with the respective bulk interchain C–C rdf, there are significant differences in interchain carbon packing [Fig. 11(b)], namely, carbon arrangements in bulk PEO show a clear gradation of nearest neighbors (first peak) and second neighbors (shoulder to the first peak) as dictated by the arrangement of carbons and oxygen in the PEO monomer [(—O—C—C—)$_n$]. Moreover, there is a definite second peak that is markedly suppressed in the confined chains. This overall behavior was unaltered over the entire temperature range that we investigated, encompassing regions well below and above the melting temperature of bulk PEO. However, rdfs of confined PEO across the slit displayed just one peak, a result of the bilayer structure in the slit. The rdf in confinement also quickly smoothed out, showing a distinct absence of bulk (liquidlike or crystalline) arrangement. This result, in light of the previous discussion, strengthened our belief that the effect of the nanoscopic confinement on the polymer chains is to inhibit any degree of preferential order and packing between the various chains in the system. Confinement does not, however, affect the packing within a chain. For example, a comparison of the intrachain carbon–carbon rdfs (Fig. 12) between bulk and confined systems showed no substantial difference, confirming that confinement does not affect the packing of atoms across the chain, which is completely dictated by the bonded interactions (for small distances).
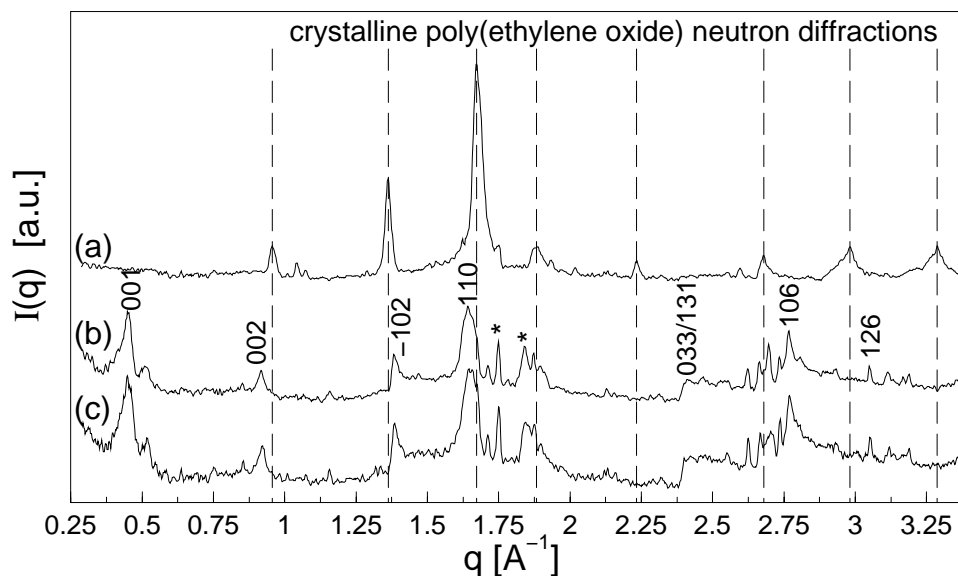
Figure 13. Wide Angle Neutron Diffraction (WAND) of PEO (a, 298K) and of purely intercalated PEO/MMT (b, 298 K; c, 15 K). For the intercalates (b,c) the known reflections of MMT are also indexed, those with conflicting *hkl* indexing are marked by a *. The disappearance of the crystalline PEO diffraction peaks is indicative of loss of polymer crystallinity upon intercalation in the MMT.

Simulation Insights Compared Against Experimental Studies

These simulation results are in concert with studies focusing on PEO thin-film morphology, for example, the work by Reiter and coworkers[48–51] on ultrathin (monolayer) films of crystalline PEO on a silicon oxide substrate. In those studies, atomic force microscopy experiments reported that the minimum height for crystal finger development is about 8 nm, considerably larger than the size of a single PEO helix and the size of our slit pore. Moreover, our conclusions are also in concert with experimental (DSC and Thermally Stimulated Current, TSC) studies on intercalated PEO, which showed no evidence of a polymer melting transition in confined PEO systems.[4] Finally, our conclusion that the intercalated PEO is disordered/not crystalline can also be checked experimentally by diffraction and calorimetry studies. Figure 13 shows the WAND of neat PEO [Fig. 13(a)] and of a purely intercalated PEO/MMT nanocomposite [Fig. 13(b,c)]. The neat PEO polymer was examined at room temperature (298 K), whereas two WAND runs were done for the intercalates at temperatures of 15 K and 298 K to delineate any effects of thermal noise. It is apparent that upon intercalation all the crystalline PEO reflections disappear, indicative of the loss of PEO crystallinity in the confined/intercalated geometry.

On a more quantitative approach, we measured the enthalpy of melting in PEO/MMT systems (Fig. 14) across the whole range of MMT loadings; this is an informative study because these PEO/MMT nanocomposites retain the same intercalated structure across the whole ϕ_{MMT} range[47] (Fig. 1). If our aforementioned discussion is valid, for purely intercalated systems ($\phi_{MMT} \geq 0.75$, i.e., all the PEO exists within the MMT intergalleries) there is no enthalpy of melting detected; this is in concert with the WAND data (Fig. 13) which show an absence of PEO diffractions in the intercalates. Also, with increasing MMT content in the PEO matrix, the fraction of the polymer that becomes intercalated is proportionally increased (as $0.33 \cdot \phi_{MMT}$), and the enthalpy of melting is expected to decrease linearly with ϕ_{MMT} following the dotted line in Figure 14. Our experimental studies showed exactly these trends—no enthalpy of melting for $\phi_{MMT} \geq 0.75$. Also, the slope of the experimental line closely follows the slope of the simulation prediction, that is, the crystallizable fraction of PEO reduces proportionally to the amount of PEO that becomes intercalated between the MMT layers. The fact that the experimental points were systematically higher than the simulation prediction by a constant enthalpy per PEO mass reflects the change
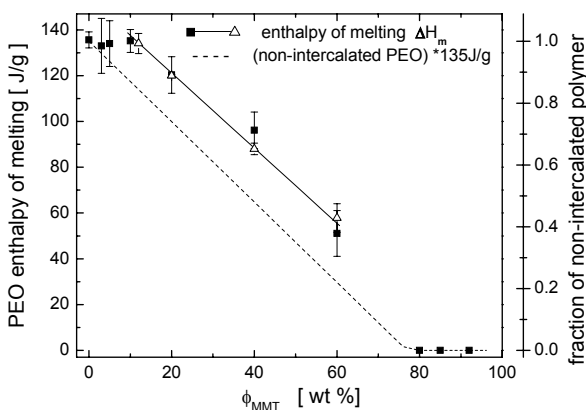
Figure 14. Experimental enthalpies of melting for PEO/MMT nanocomposites, from ref. [52]. The data were collected by differential scanning calorimetry from the second heating cycle at a rate of 10°C/*min*. The dotted line denotes the prediction that any PEO that becomes intercalated does not crystallize [i.e., it is assumed that the intercalated polymer fraction has zero enthalpy of melting and the nonintercalated PEO fraction has the bulk (unfilled) enthalpy of melting]. The systematic deviation of the experiments above the dotted line was caused by the effects of the MMT on the PEO enthalpy of fusion and the PEO crystal morphology (see, e.g., ref. 47).

of the PEO crystal morphology and the change of PEO's enthalpy of fusion in the presence of the MMT fillers,[47,52] that is, it reflects the crystal changes of the PEO outside the MMT tactoids.

CONCLUSIONS

MD computer simulations were used to examine the structure of PEO in nanoscopic confinement. Focusing on PEO/MMT intercalated systems and comparing against bulk PEO, the confined polymers exhibit distinctly amorphous features across a wide temperature range, with no indication of any crystalline or periodic arrangement. This challenges the traditional picture for intercalated PEO but is in concert with the experimental studies. Indicatively, our simulation-derived 1D electron densities agree with the experimental XRD studies; the simulation predictions for amorphous conformations in the intercalates are confirmed by WAND showing a suppression of the PEO crystalline peaks upon intercalation and DSC studies measuring a systematic decrease of melting enthalpy with MMT in PEO/MMT composites closely following the mass of PEO intercalated between the MMT layers. Multiple order parameters calculated from the simulations of MMT-

intercalated PEO show the confined systems to be less ordered than the most disordered bulk across all temperatures simulated (273–423 K). These disordered PEO arrangements are attributed to confinement-induced effects on the chain–chain packing and to the oxygen/Li coordination in the interlayer galleries.

APPENDIX

Mathematically, the intensity of the XRD peaks can be represented as follows

$$I(\theta) = \phi(\theta)LP(\theta)G^2(\theta) \qquad \text{(A1)}$$

where θ is the angle of diffraction, I is the intensity of the diffraction peaks, $\phi(\theta)$ is the interference function, $LP(\theta)$ is the Lorenz polarization factor, and $G(\theta)$ is the structure factor.

The interference function depends on the coherence length across the corresponding diffracting *hkl* planes. It is the ideal signal that would evolve if the system under consideration was made up of identical point particles interacting with the X-ray beam. In reality, this ideal response is modified because of the presence of atoms of different size electron clouds, by crystallites of different sizes, and by instrumental errors. Taking all these factors into account, experimentally derived XRD peaks were of varying intensities and widths, although at the same angle (θ) as in the ideal case.

For systems with centers of symmetry in the *c* direction of the lattice, the structure factor at any angle θ is given by

$$G(\theta) = \sum_n P_n f_n \cos(4\pi z_n \sin\theta/\lambda) \qquad \text{(A2)}$$

where the summation extends over all n types of atoms in one unit cell with their z coordinates represented by z_n, P_n is the number of n atoms present in the unit cell, and f_n is the appropriate temperature corrected scattering factor. Standard values for

all the terms were taken from the literature, and the structure amplitudes were calculated.

The Lorenz polarization factor is a combination of two terms: the Lorenz factor, which depends on the particle orientation and geometric factors inherent in the measuring of diffraction intensities, and the polarization factor, which quantifies the loss of intensity because of the unpolarized nature of the incident X-ray beam. The contributions of all these different factors to the diffracted intensities are lumped together into one term as follows:

$$LP(\theta) = \frac{1 + \cos^2\theta}{\sin^2\theta \cos\theta} \qquad \text{(A3)}$$

The XRD peak intensities that correspond to Cu Kα XRD diffraction by our simulation unit cell were all verified with ones calculated with the "WinStruc" software.

REFERENCES AND NOTES

1. Alexandre, M.; Dubois, P. Mater Sci Eng R: Rep 2000, 28, 1.
2. Giannelis, E. P.; Krishnamoorti, R.; Manias, E. Adv Polym Sci 1999, 138, 107.
3. Wu, J.; Lerner, M. M. Chem Mater 1993, 5, 835.
4. Vaia, R. A.; Sauer, B. B.; Tse, O. K.; Giannelis, E. P. J Polym Sci Part B: Polym Phys 1997, 35, 59.
5. Aranda, P.; Ruiz-Hutsky, E. Chem Mater 1992, 4, 1395.
6. Wong, S.; Vaia, R. A.; Giannelis, E. P.; Zax, D. B. Solid State Ionics 1996, 86, 547.
7. Yang, D. K.; Zax, D. B. J Chem Phys 1999, 110, 5325.
8. Vaia, R. A.; Vasudevan, S.; Krawiec, W.; Scanlon, L. G.; Giannelis, E. P. Adv Mater 1995, 7, 154.
9. Wang, L.; Rocci-Lane, M.; Brazis, P.; Kannewurf, C. R.; Kim, Y.; Lee, W.; Choy, J.; Kanatzidis, M. G. J Am Chem Soc 2000, 122, 6629.
10. Anastasiadis, S. H.; Karatasos, K.; Vlachos, G.; Giannelis, E. P.; Manias, E. Phys Rev Lett 2000, 84, 915.
11. Manias, E.; Chen, H.; Krishnamoorti, R.; Genzer, J.; Kramer, E. J.; Giannelis, E. P. Macromolecules 2000, 33, 7955.
12. Hackett, E.; Manias, E.; Giannelis, E. P. Chem Mater 2000, 12, 2161.
13. Kuppa, V.; Manias, E. Chem Mater 2002, 14, 2171.
14. Kuppa, V.; Manias, E. J Chem Phys 2003, 118, 3421.
15. Lee, J. Y.; Baljon, A. R. C.; Loring, R. F. J Chem Phys 1999, 111, 9754.
16. Manias, E.; Kuppa, V.; Yang, D. K.; Zax, D. B. Colloids Surf 2001, 187, 509.
17. Manias, E.; Kuppa, V. Eur Phys J E 2002, 8, 193.
18. Theng, B. K. G. Formation and Properties of Clay Polymer Complexes; Elsevier: New York, 1979.
19. Smith, G. D.; Jaffe, R. L.; Yoon, D. Y. J Phys Chem 1993, 97, 12752.
20. Smith, G. D.; Jaffe, R. L.; Yoon, D. Y. J Am Chem Soc 1995, 117, 530.
21. Torini, I. G.; Sperb, R.; Smith, P. E.; van Gunsteren, W. F. J Chem Phys 1995, 102, 5451.
22. Chávez-Páez, M.; Van Workum, K.; de Pablo, L.; de Pablo, J. J. J Chem Phys 2001, 114, 1405.
23. Londano, J. D.; Annis, B. K.; Habenschuss, A.; Borodin, O.; Smith, G. D.; Turner, J. Z.; Soper, A. K. Macromolecules 1997, 30, 7151.
24. Smith, G. D.; Yoon, D. Y.; Jaffe, R. L.; Colby, R. H.; Krishnamoorti, R.; Fetters, L. J. Macromolecules 1996, 29, 3462.
25. Berendsen, H. J. C.; Postma, J. P. M.; van Gunsteren, W. F.; DiNola, A.; Haak, J. R. J Chem Phys 1984, 81, 3684.
26. Müller-Plathe, F. Acta Polym 1994, 45, 259.
27. Müller-Plathe, van Gunsteren, W. F. J Chem Phys 1995, 103, 4745.
28. Londano, J. D.; Annis, B. K.; Habenschuss, A.; Borodin, O.; Smith, G. D.; Turner, J. Z.; Soper, A. K. Macromolecules 1997, 30, 7151.
29. Annis, B. K.; Kim, M. H.; Wignall, G. D.; Borodin, O.; Smith, G. D. Macromolecules 2000, 33, 7544.
30. Wang, L.; Kanatzidis, M. G. Chem Mater 2001, 13, 3717.
31. Vaia, R. A. Polymer-Clay Nanocomposites; Wiley: New York, 2001; pp 229.
32. Liu, Y. J.; Schindler, J. L.; DeGroot, D. C.; Kannewurf, C. R.; Hirpo, W.; Kanatzidis, M. G. Chem Mater 1996, 8, 525.
33. Chaiko, D. J. Chem Mater 2003, 15, 1105.
34. Israelachvili, J. Intermolecular and Surface Forces; Academic: New York, 1991.
35. Christenson, H. K. J Chem Phys 1983, 78, 6906.
36. Chan, D. Y. C.; Horn, R. G. J Chem Phys 1985, 83, 5311.
37. Montfort, J. P.; Hadziioannou, G. J Chem Phys 1988, 88, 7187.
38. Gee, M. L.; McGuiggan, P. M.; Israelachvili, J. N.; Homola, A. M. J Chem Phys 1990, 93, 1895.
39. van Alsten, J.; Granick, S. Macromolecules 1990, 23, 4856.
40. Granick, S. Science 1991, 253, 1374.
41. Hu, H.; Carson, G. A.; Granick, S. Phys Rev Lett 1991, 66, 2758.
42. Klein, J.; Kumacheva, E. Science 1995, 269, 816.
43. Errington, J. R.; Debenedetti, P. G. Nature 2001, 409, 318.
44. ten Wolde, P. R.; Ruiz-Montero, M. J.; Frenkel, D. J Chem Phys 1996, 104, 9932.
45. Chau, P. L.; Hardwick, A. J. Mol Phys 1998, 93, 511.
46. Steinhardt, P. J.; Nelson, D. R.; Ronchetti, M. Phys Rev B 1983, 28, 784.
47. Strawhecker, K.; Manias, E. Chem Mater 2003, 15, 844.
48. Reiter, G.; Sommer, J. Phys Rev Lett 1998, 80, 3771.
49. Reiter, G.; Sommer, J. J Chem Phys 2000, 112, 4376.
50. Sommer, J.; Reiter, G. J Chem Phys 2000, 112, 4384.
51. Reiter, G. J Polym Sci Part B: Polym Phys 2003, 41, 1869.
52. Menakanit, S. M. Sc. Thesis, Penn State University, 2002.